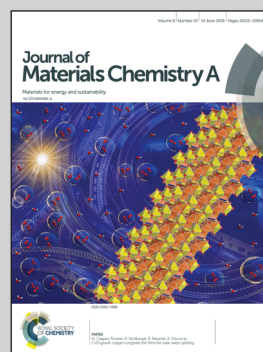


Introduction of SnO₂-modified TiO₂ films towards high-efficiency planar perovskite solar modules by Prof. Guan-Jun Yang *et al.* at State Key Laboratory for Mechanical Behavior of Materials, School of Materials Science & Engineering, Xi'an Jiaotong University, P. R. China.

Low-temperature SnO₂-modified TiO₂ yields record efficiency for normal planar perovskite solar modules

Low-temperature SnO₂-modified TiO₂ yields record efficiency for normal planar perovskite solar modules. A novel electron transport layer synthesised *via* chemical bath with a dense and uniform morphology has been applied to enhance electron extraction, thus boosting the large-scale fabrication and record efficiency for normal planar perovskite solar modules.

As featured in:



See Guan-Jun Yang *et al.*,
J. Mater. Chem. A, 2018, **6**, 10233.



rsc.li/materials-a


Registered charity number: 207890

PAPER



Cite this: *J. Mater. Chem. A*, 2018, 6, 10233

Low-temperature SnO₂-modified TiO₂ yields record efficiency for normal planar perovskite solar modules†

Bin Ding, Shi-Yu Huang, Qian-Qian Chu, Yan Li, Cheng-Xin Li, Chang-Jiu Li and Guan-Jun Yang *

Hybrid organic–inorganic perovskite solar cells (PSCs), particularly planar PSCs, have attracted significant attention because of their high efficiency, low fabrication costs, and simple preparation process. However, planar PSCs exhibit lower efficiency and stability than mesoporous PSCs primarily owing to defects in the electron transport layer (ETL). Herein, we introduced a SnO₂ nanoparticle-modified TiO₂ film (SnO₂@TiO₂) as an ETL. In addition, we proposed a simple three-step chemical bath method to achieve this SnO₂@TiO₂ structure at low temperatures (140 °C). The SnO₂@TiO₂ ETL significantly enhances electron extraction and decreases the trap states at the perovskite/ETL interface. We achieved average efficiencies of 21.27%, 19.79%, 17.21%, and 16.31% at the reverse scan and forward scan for the device areas of 0.10 cm², 1.13 cm², 5.25 cm², and 10.56 cm², respectively. Moreover, we achieved a certificated efficiency of 15.65% for a normal planar perovskite solar module with a masked area of 10.55 cm². The SnO₂@TiO₂-based PSCs exhibit enhanced photocurrent and reduced hysteresis. Furthermore, the solar cell retained about 89% of its initial efficiency after about 750 hours of aging in dark and about 93% for 528 hours under full-sun illumination. Owing to the low-temperature processability and the absence of spin-coating steps, SnO₂@TiO₂ ETLs will provide a promising path for the commercialization of PSCs.

Received 5th February 2018
Accepted 13th March 2018

DOI: 10.1039/c8ta01192c

rsc.li/materials-a

Introduction

Advanced hybrid organic–inorganic lead halide materials have boosted the power conversion efficiency (PCE) of perovskite-based solar cells (PSCs) from 3.8% to 22.7% for devices with area under 1 cm² (ref. 1–4) and more than 23% for silicon–perovskite tandem cells.^{5,6} Due to their low cost and remarkably high efficiency, PSCs are on the way from the research laboratory to commercial production,⁷ and problems such as long-term stability and large-area fabrication of devices are being gradually solved by tuning the perovskite component,^{4,8,9} controlling crystal nucleation and growth,^{10–13} applying stable electron transport layers^{14–16} or using hydrophobic materials to protect the perovskite.^{17,18} Normally, stable and high-efficiency PSCs require a mesoporous scaffold (such as TiO₂) that needs a high-temperature (>450 °C) process, and it is difficult to deposit this scaffold at a uniform thickness of ~150 nm by spin-coating on large areas.^{9,10,12,19} However, the mesoporous scaffold can be removed in planar heterojunction structure PSCs, where

the perovskite absorber is sandwiched between the electron transport layer (ETL) and the hole transport material (HTM).²⁰ The planar device structure further evolved into an n–i–p structure, known as the normal planar device structure, and a p–i–n structure, known as the inverted device structure,^{21,22} which attracted significant attention for their low-temperature fabrication process and roll-to-roll manufacturing procedure.^{23–26} However, the PCE of the normal planar PSCs is significantly lower than that of the mesoporous-type PSCs; this may be due to increased charge recombination caused by the short diffusion length of electrons.²⁷ In general, the high-efficiency normal planar PSCs typically use a compact TiO₂ layer as the ETL, which is deposited *via* spin-coating followed by a low-temperature (<150 °C) treatment^{28,29} or high-temperature (>450 °C) sintering.³⁰ However, the spin-coated TiO₂ layers have a very unequal thickness because of the rough surface of the FTO layer; this causes an ineffective electron transfer where the TiO₂ layer is too thick and a severe recombination where the TiO₂ layer is too thin.³¹ The spin-coated ETL can result in a relatively lower efficiency of the planar PSCs due to thickness nonuniformity and imperfect contact with the substrate. Moreover, the device area of most normal planar PSCs is less than 0.2 cm² (ref. 28–30) possibly due to size limitations of the spin-coating process. Spray pyrolysis is a promising large-scale manufacturing approach for the TiO₂ ETL; however, it still

State Key Laboratory for Mechanical Behavior of Materials, School of Materials Science & Engineering, Xi'an Jiaotong University, No. 28, Xianning West Road, Xi'an, Shaanxi, 710049, P. R. China. E-mail: ygj@mail.xjtu.edu.cn

† Electronic supplementary information (ESI) available. See DOI: 10.1039/c8ta01192c

requires a high-temperature sintering at up to 450 °C, and the conversion efficiency is only 16.3% for devices based on the TiO₂ ETLs fabricated by spray pyrolysis with device area larger than 1 cm².^{32,33}

Another important issue of concern is the serious hysteresis existing in the normal planar PSCs. The mechanism of the hysteresis phenomena is attributed to several effects such as ion migration^{34–37} or trapping of electrons at the interfaces.^{36,38–40} In planar PSCs with TiO₂ ETLs, the trapping of electrons at the TiO₂/perovskite interface significantly affects the hysteresis more than that at the perovskite/spiro-OMeTAD interface because of the low electron mobility of TiO₂ ETL and the trap states appearing at the TiO₂ surface, especially upon exposure to UV light.^{41–43} To overcome these drawbacks, various modifications of the TiO₂ ETL have been proposed such as using a fullerene self-assembled monolayer to passivate the TiO₂ surface,⁴⁴ using phosphotungstic acid to obtain a better band alignment between the TiO₂ and the perovskite,⁴⁵ and using the 1-butyl-3-methylimidazolium tetrafluoroborate ionic liquid to reduce the density of traps.³⁰ However, in an unexpected development, Tan *et al.* have recently applied chlorine-capped TiO₂ nanocrystal films as ETLs, significantly reducing the interface recombination, thus achieving a certified efficiency of 19.5% without hysteresis for 1.1 cm² devices.²⁶ However, the process of preparation of the chlorine-capped TiO₂ ETL is complexed by the wet-chemical method involving several steps such as heating at 85 °C for 12 hours, chemical precipitation by the addition of diethyl ether, and centrifugation for three times. These results imply that the trap states at the TiO₂/perovskite interface are indeed one of the reasons for the hysteresis existing in planar PSCs.

Recently, SnO₂ has been reported to be a promising candidate to decrease or even eliminate hysteresis in normal planar PSCs^{25,46,47} because of its low-temperature solution fabrication process, more efficient electron transfer ability (even faster than that of TiO₂),⁴⁸ better alignment of the conduction band to perovskite,⁴⁹ and faster electron extraction.²⁵ However, to date, the SnO₂ ETL is mostly fabricated by spin coating for high-efficiency PSCs and the so-called low temperature reaches up to 180 °C, which is still too high for the flexible solar cells.^{46,47} Recently, SnO₂ ETLs combined with potassium-containing quadruple-cation perovskite have achieved an efficiency of 15.76% without hysteresis for normal planar perovskite solar modules;⁵⁰ this indicates that SnO₂ ETLs have enormous potential.

In this study, we introduced a SnO₂ nanoparticle-modified TiO₂ film (SnO₂@TiO₂) as the ETL for normal planar PSCs. Moreover, a three-step chemical bath method has been proposed to deposit SnO₂@TiO₂ on the FTO substrate, which can yield high-quality and highly reproducible SnO₂@TiO₂ films. The TiO₂ compact layer was first deposited on the substrate *via* a two-step chemical bath method at low temperatures, not exceeding 120 °C. Next, SnO₂ was deposited on the TiO₂ film *via* a three-step chemical bath method at a temperature less than 140 °C. The results indicate that the SnO₂@TiO₂ ETL can significantly enhance electron extraction and decrease the trap states at the ETL/perovskite interface. Then, upon

combining this technique with our previous method for producing high-quality and large-scale perovskite films,^{10,13} we achieved average efficiencies of 21.27%, 19.79%, 17.21%, and 16.31% at the reverse scan and forward scan for the active device areas of 0.10 cm², 1.13 cm², 5.25 cm², and 10.56 cm², respectively. More importantly, an average PCE of 15.65% was certified by the PV test laboratory of Newport Corporation PV Lab (one of the six worldwide-recognized certification bodies), a record certificated efficiency for normal planar perovskite solar modules and second only to 17.4% (ref. 51) for perovskite solar modules certificated by the same certification body.

Results and discussion

The TiO₂ nanoparticle film deposited on the FTO substrate normally presents pinholes/voids, which produce a direct contact between perovskite and FTO and cause severe recombination. To avoid pinholes/voids, we fabricated TiO₂ films using a two-step chemical bath method. Since many trap states are located at the perovskite/TiO₂ interface, SnO₂ nanoparticles have been added to the TiO₂ film, separating the perovskite from TiO₂ (Fig. 1a). As shown in Fig. 1b, the FTO substrate was first soaked in the TiCl₄ solution, having a relatively high concentration of 200 mM, that is normally used to treat the TiO₂ mesoporous layer in mesoporous-type perovskite solar cells.⁵² Then, the substrate was soaked in a 20 mM TiCl₄ solution with the aim to further increase the density of the film obtained in the previous step. Sequentially, the substrate was soaked in the SnCl₂ solution. The temperature of the chemical bath during the abovementioned three steps was 70 °C. Finally, the substrate was annealed at 140 °C. All experimental details are given in the ESI† After the FTO substrates were sequentially soaked in a high-concentration TiCl₄ (H-TiCl₄) solution, low-concentration TiCl₄ (L-TiCl₄) solution, and SnCl₂ solution, the surfaces of the FTO crystals were fully covered with nanoparticles, and the crystals retained their rough surface topology, *i.e.*, the nanoparticle films uniformly covered the FTO film in a conformal manner (Fig. 1c–f). The morphology of the TiO₂ film grown from the H-TiCl₄ solution (Fig. 1d) remains unaltered after treatment with a L-TiCl₄ solution (Fig. 1e) and SnCl₂ solution (Fig. 1f). To observe the film grown from L-TiCl₄ and SnCl₂ solutions, the FTO substrates were directly soaked in the L-TiCl₄ solution (Fig. 1g) and SnCl₂ solution (Fig. 1h). It is obvious that the nanoparticle films generated from H-TiCl₄ solution (Fig. 1d) are thicker than those generated from L-TiCl₄ solution (Fig. 1g)⁴¹ and SnCl₂ solution (Fig. 1h). The hydrolysis products of TiCl₄ are normally regarded as hydrous titanium oxides;⁵³ therefore, the TiO₂ film prepared by the chemical bath method is subsequently annealed at 120 °C to dehydrate hydrous titanium oxides. This would shrink the TiO₂ film and lead to the generation of pinholes. However, the pinholes were then filled by the treatment of L-TiCl₄ solution.

X-ray photoelectron spectroscopic (XPS) measurements reveal the composition of the films obtained from the hydrolysis of TiCl₄ and SnCl₂. The full XPS spectra are shown in Fig. S1a (ESI†). In the XPS spectra of Ti, O, and Sn elements (Fig. 2a–c), TiO₂ is observed,⁵⁴ whereas SnO₂ is absent for the TiO₂/FTO

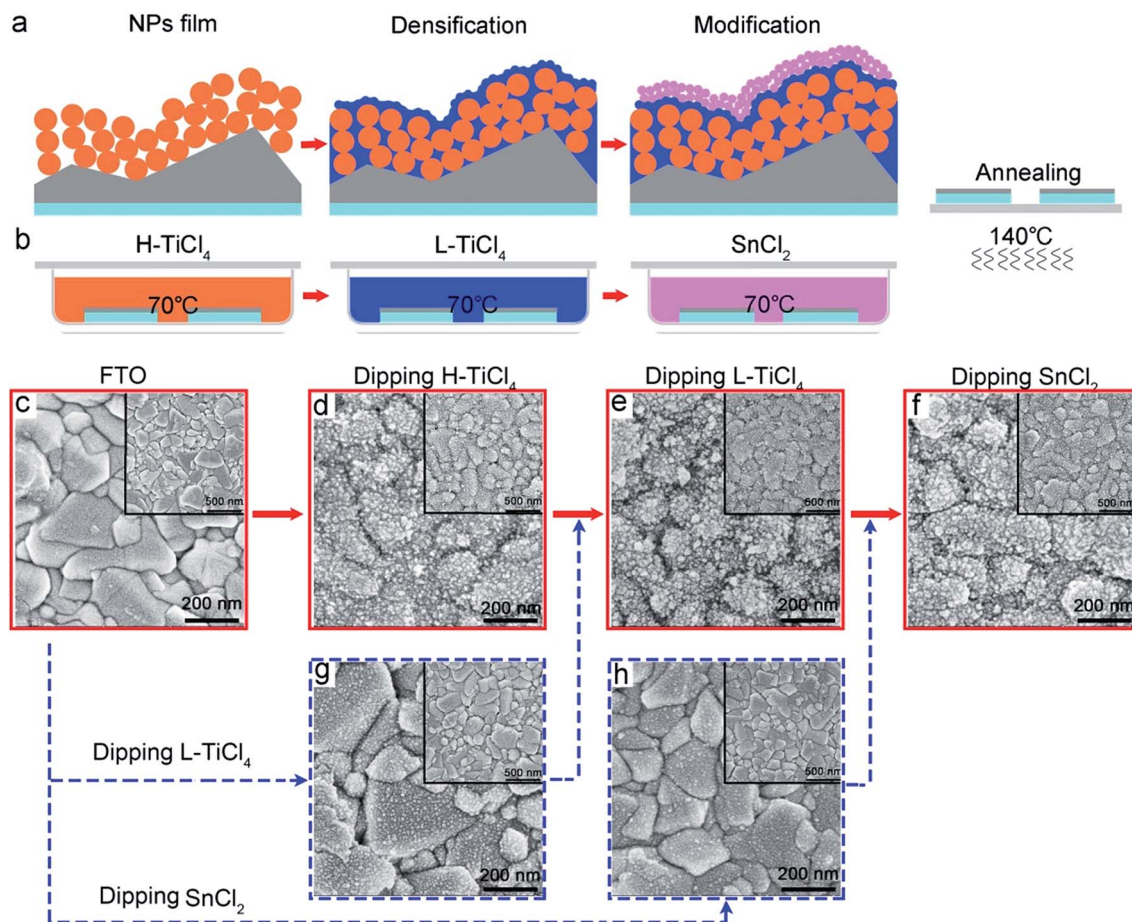


Fig. 1 Schematic and microscopy images. (a) The designed structure of the $\text{SnO}_2@/\text{TiO}_2$ film. (b) Fabrication process of the $\text{SnO}_2@/\text{TiO}_2$ film by the three-step chemical bath method from left to right. Low- and high-magnification top-view SEM images of morphology evolution of the ETL from the original FTO film to the final $\text{SnO}_2@/\text{TiO}_2$ film, (c) the FTO substrate, (d) the FTO substrate treated with the H-TiCl_4 solution, (e) the FTO substrate first treated with H-TiCl_4 and then treated with L-TiCl_4 , (f) the FTO substrate sequentially treated with H-TiCl_4 , L-TiCl_4 , and SnCl_2 solution, (g) the FTO substrate treated with the L-TiCl_4 solution, and (h) the FTO substrate treated with the SnCl_2 solution.

film; this indicates that the TiO_2 film completely covers the FTO substrate. Moreover, two small peaks of Ti^{4+} are observed in the $\text{SnO}_2@/\text{TiO}_2/\text{FTO}$ films (Fig. 2a), which can be attributed to the very small thickness of the SnO_2 layer. All $\text{SnO}_2@/\text{TiO}_2/\text{FTO}$ films annealed at different temperatures exhibited two strong Sn^{4+} peaks at 495.3 eV and 487.0 eV without any Sn^{2+} peaks (Fig. 2b); when combined with the oxygen peak O 1s observed at 531.0 eV (Fig. 2c), this result demonstrated that pure SnO_2 films were successfully prepared using the $\text{SnCl}_2 \cdot 2\text{H}_2\text{O}$ precursor. Therefore, we could significantly decrease the temperature for the preparation of the SnO_2 film from SnCl_2 to 80 °C, whereas in the previously reported processes, the temperature was almost up to 180 °C.^{46,47} We can ascribe the successful results obtained even at this lower temperature to the oxidation of Sn^{2+} to Sn^{4+} by oxygen dissolved in the SnCl_2 solution during the hydrolysis procedure at 70 °C and to the very small thickness of the freshly prepared film obtained from SnCl_2 that allows an effective oxidation of the SnO_2 film by oxygen in the air during the subsequent annealing process. The X-ray diffraction (XRD) patterns obtained for the abovementioned films are shown in Fig. S1b (ESI[†]), and they indicate that no other peaks of metallic

oxide phases are found in FTO. According to the transmission spectra, both the TiO_2 film and $\text{SnO}_2@/\text{TiO}_2$ film obtained by the chemical bath method hardly affect the transparency of the FTO substrate in the visible region (Fig. S1c, ESI[†]); this may be due to the very small thickness of the TiO_2 film and $\text{SnO}_2@/\text{TiO}_2$ film. Moreover, the SnO_2 layer has little influence on the electrical conductance of the TiO_2 electron transport layer obtained directly from the slope of the $I-V$ curves of the FTO/ETL/Au devices (Fig. S1d, ESI[†]). UV-vis absorption spectra of the perovskite ($(\text{FAPbI}_3)_{0.3}(\text{MAPbI}_3)_{0.7}$) films deposited on FTO, TiO_2/FTO , and $\text{SnO}_2@/\text{TiO}_2/\text{FTO}$ substrates were obtained, and all the spectra exhibited the typical perovskite absorption spectra with a sharp absorption onset at 800 nm (Fig. 2d).

To study the charge transfer properties, steady photoluminescence (PL) and time-resolved photoluminescence (TRPL) were measured. As shown in Fig. 2e, the perovskite film on $\text{SnO}_2@/\text{TiO}_2$ exhibits an enhanced PL quenching in comparison with that on the TiO_2 film. The TRPL data were fitted using bi-exponential decay to obtain the decay lifetime for the slow recombination process that means recombination at the ETL/perovskite interface. The perovskite film deposited on

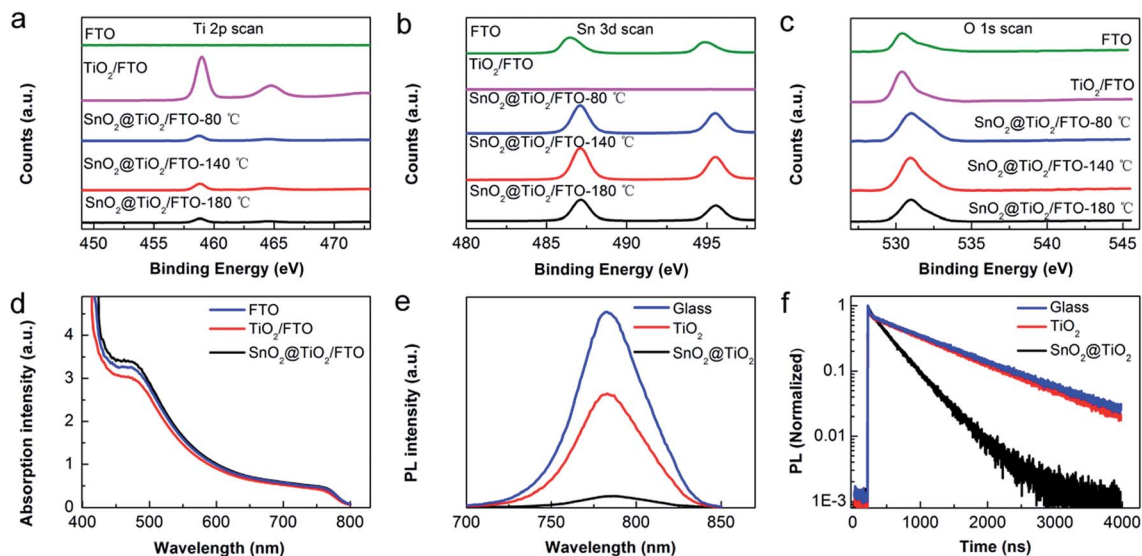


Fig. 2 XPS spectra, UV-vis spectra, photoluminescence spectra, as well as time-resolved photoluminescence. XPS spectra of (a) Ti 2p scan, (b) Sn 3d scan, and (c) O 1s scan of the FTO substrate, the TiO_2/FTO film, and the $\text{SnO}_2@\text{TiO}_2/\text{FTO}$ films annealed at a temperature of 80, 140, and 180 °C, respectively. (d) The UV-vis spectra of the perovskite films deposited on the FTO substrate, the TiO_2/FTO film, and the $\text{SnO}_2@\text{TiO}_2/\text{FTO}$ film. (e) PL and (f) TRPL for the perovskite films deposited on the glass, the TiO_2 film, and the $\text{SnO}_2@\text{TiO}_2$ film deposited on the glass.

the $\text{SnO}_2@\text{TiO}_2$ film shows a lifetime of 174 ns, much shorter than 536 ns and 448 ns for the glass and TiO_2 films, respectively. Moreover, the electron diffusion coefficient was estimated by fitting the TRPL data with the eqn (S1) (ESI[†]). The electron diffusion coefficient is $4.3 \times 10^{-3} \text{ cm}^2 \text{ s}^{-1}$ for the perovskite film deposited on the $\text{SnO}_2@\text{TiO}_2$ film, much larger than $2.19 \times 10^{-3} \text{ cm}^2 \text{ s}^{-1}$ for the perovskite film deposited on the TiO_2 film. As observed from the PL and TRPL results, the $\text{SnO}_2@\text{TiO}_2$ film displays a fast electron transfer and an efficient electron band alignment between the SnO_2 film and the perovskite film.

Fig. 3a shows the cross-sectional SEM image of perovskite/ $\text{SnO}_2@\text{TiO}_2/\text{FTO}$. More images of the morphology of the perovskite films deposited on TiO_2 or $\text{SnO}_2@\text{TiO}_2$ are shown in Fig. S2 (ESI[†]). It can be clearly observed that TiO_2 or $\text{SnO}_2@\text{TiO}_2$ nanoparticle films grow in a conformal manner on the surface of the FTO substrates and form thin, uniform, and pinhole-free blocking layers, closely connected to the substrate. Moreover, the perovskite films grow conformally on the TiO_2 or $\text{SnO}_2@\text{TiO}_2$ films, showing dense, uniform, and pinhole-free morphology. The XRD spectra show that perovskite films with or without annealing on TiO_2 or $\text{SnO}_2@\text{TiO}_2$ exhibit a pure tetragonal phase free of PbI_2 (Fig. S3, ESI[†]).⁵⁵ However, many details about the $\text{SnO}_2@\text{TiO}_2$ nanoparticle films remain unclear due to the nanoscale sizes of the particles and film thickness (about 40 nm, as estimated from the SEM image shown in Fig. 3a). Therefore, high-resolution transmission electron microscopy (TEM) was employed to characterize the distribution of SnO_2 nanoparticles on the TiO_2 film, the $\text{SnO}_2@\text{TiO}_2/\text{FTO}$ interface, and the exact thickness of the $\text{SnO}_2@\text{TiO}_2$ film. Fig. 3b shows high-angle annular dark field (HAADF) scanning cross-sectional-view TEM image of the perovskite film deposited on the $\text{SnO}_2@\text{TiO}_2/\text{FTO}$ substrate; the corresponding low-

magnification image is shown in Fig. S4a (ESI[†]). The magnified cross-sectional TEM image shows an explicit view of the $\text{SnO}_2:\text{F}$ (FTO)/ $\text{SnO}_2@\text{TiO}_2$ interface and the $\text{SnO}_2@\text{TiO}_2$ /perovskite interface, demonstrating a close contact among the three layers (Fig. S4b[†]). Individual elemental maps of F, O, Sn, and Ti for the area indicated by the white box in Fig. 3b clearly outline the $\text{SnO}_2:\text{F}/\text{SnO}_2@\text{TiO}_2$ interface and show the existence of SnO_2 (Fig. 3c–f). Other elemental maps of C, N, I, and Pb are shown in Fig. S4c–f (ESI[†]). The energy-dispersive spectra for two points reveal the existence of SnO_2 (Fig. S4g–i, ESI[†]). As shown in Fig. 3g, the thickness of $\text{SnO}_2@\text{TiO}_2$ is ~ 30 nm, significantly thinner than that of the ETLs described in the literature,^{26,28} but thick enough to form a compact layer due to the three-step sequential chemical bath method that forms extremely small nanoparticles (Fig. 1). An atomic resolution TEM image shows clear lattice fringes, thus revealing a clear interface indicated by the white line at the atomic scale (Fig. 3h). A crystalline structure with a lattice spacing of 0.24 nm might be indexed as the (220) plane of FTO, further confirmed by the XRD of FTO (Fig. S3, ESI[†]). Another crystalline structure with a lattice spacing of 0.32 nm might be indexed as the (110) plane of the rutile phase of TiO_2 . Within the $\text{SnO}_2@\text{TiO}_2$ film, as shown in Fig. 3i, the randomly oriented tiny grains can be clearly observed although most grains are damaged by the Ga beam during sample preparation *via* focused ion beam; the grains exhibit small and large sizes, as outlined.

According to the abovementioned analysis, we can conclude that the thin $\text{SnO}_2@\text{TiO}_2$ film has been successfully deposited on the FTO substrate *via* the three-step chemical bath method. The $\text{SnO}_2@\text{TiO}_2$ ETL demonstrates significantly enhanced electron transfer and electron extraction, which would improve the performance of PSCs. To validate this point, we further fabricated normal planar PSCs with a structure of gold/spiro-OMeTAD/

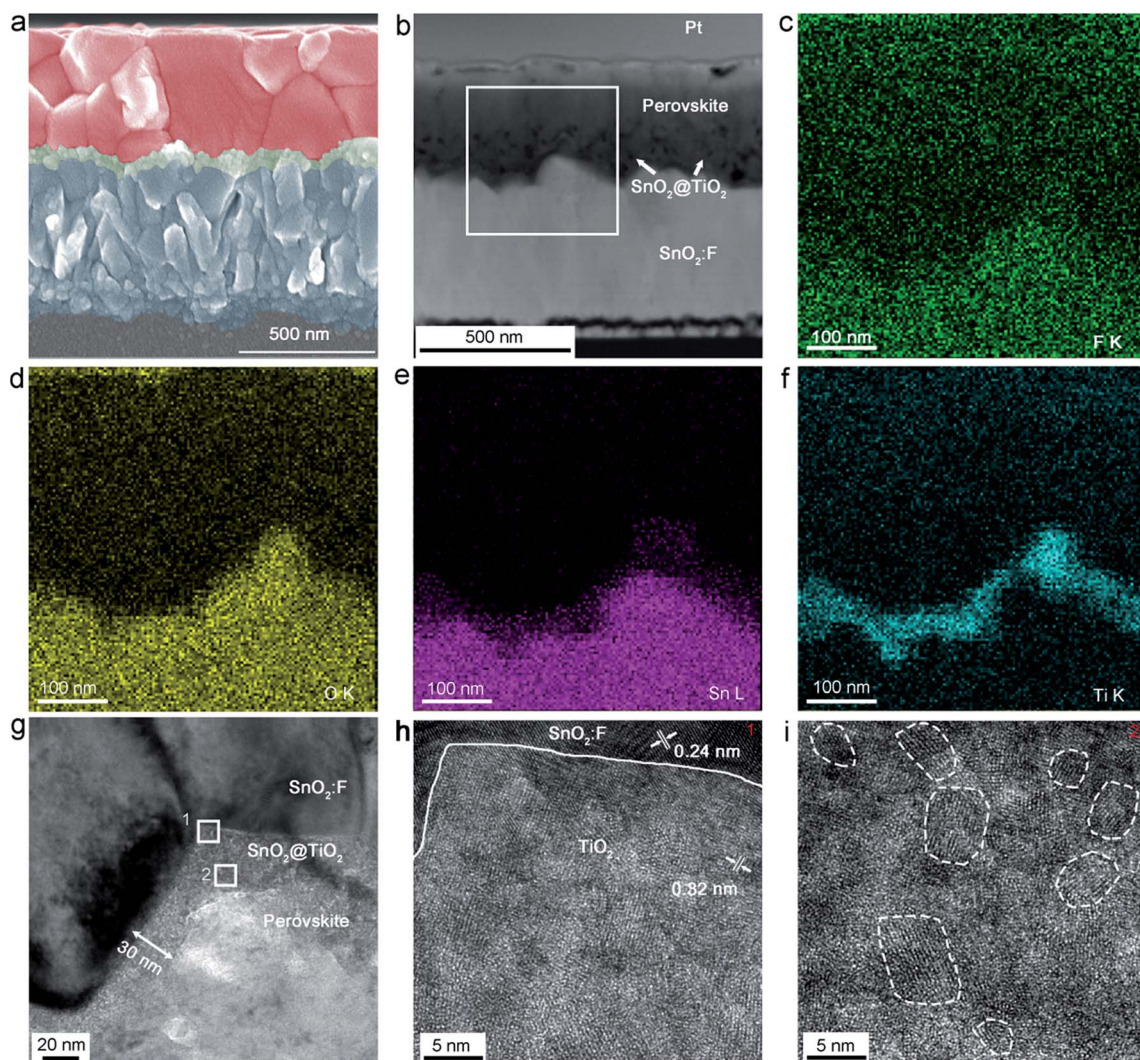


Fig. 3 TEM characterization of the perovskite/SnO₂@TiO₂/FTO (SnO₂:F) cross-sectional view. (a) Coloured cross-sectional view SEM image of the perovskite deposited on the SnO₂@TiO₂/FTO substrate. (b) HAADF scanning cross-sectional-view TEM image of the perovskite film deposited on the SnO₂@TiO₂/FTO substrate. Individual elemental maps of (c) F, (d) O, (e) Sn, and (f) Ti of the area indicated by the white box in Fig. 3b. (g) HAADF scanning TEM image of the enlarged FTO/SnO₂@TiO₂/perovskite interfaces. (h) High-resolution TEM image of the area indicated by the white box 1 in (g). (i) High-resolution TEM image of the area indicated by the white box 2 in (g) showing tiny grains outlined by dashed lines.

(FAPbI₃)_{0.3}(MAPbI₃)_{0.7}/SnO₂@TiO₂(or TiO₂)/FTO (Fig. 4a). The initial cross-sectional SEM images of the SnO₂@TiO₂-based PSCs show no differences from that of the TiO₂-based PSCs (Fig. S5, ESI[†]). The entire device was prepared at low temperatures in air at an ambient temperature of 22–25 °C and a relative humidity of 45–55%, except for the gold layer that was made by thermal evaporation. At first, SnO₂ films of different thicknesses were deposited on TiO₂ as ETLs by varying only the concentration of SnCl₂ solution with other conditions unchanged (Fig. S6a, ESI[†]). All the devices were measured with a 0.1 cm² mask under a simulated AM 1.5G solar illumination of 100 mW cm⁻² at an ambient temperature of 22–25 °C and a relative humidity of 45–55%. The corresponding photovoltaic parameters containing photocurrent density (*J*_{SC}), open-circuit voltage (*V*_{OC}), fill factor (FF), as well as PCE are listed in Table S1 (ESI[†]). We have found that the *J*_{SC} increases with the increasing concentration of

the SnCl₂ solution, but almost remains the same when the concentration is higher than 40 mM; on the other hand, the *V*_{OC} decreases if the solution concentration is too high; this is in accordance with the previous studies on cells based on the pure SnO₂ ETL.^{46,57} As already explained, the TiO₂ films were fabricated using the two-step chemical bath method, which should be dense enough to avoid the serious carrier recombination owing to the direct contact between perovskite and FTO. Thus, the enhancement in the *J*_{SC} is mainly due to the fast electron transfer and enhanced electron extraction achieved using SnO₂, which significantly alleviates charge accumulation at the trap states on the TiO₂ surface. Finally, we optimized the concentration of the SnCl₂ solution at 40 mM, at which high *J*_{SC} and *V*_{OC} could be obtained.

Thus, all the SnO₂@TiO₂ ETLs assembled into devices were then fabricated using the 40 mM SnCl₂ solution. Fig. 4b shows

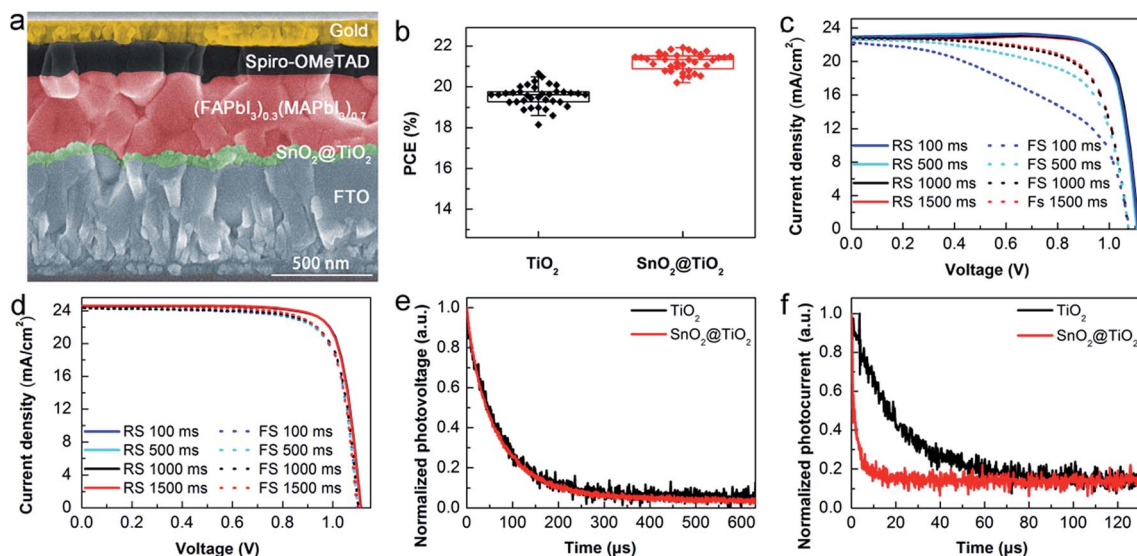


Fig. 4 SEM image and device performance. (a) Coloured cross-sectional-view SEM image of a typical normal planar perovskite solar cell with $\text{SnO}_2@\text{TiO}_2$ as ETLs. (b) Comparison of the PCE statistical graph for the devices with a masked area of 0.1 cm^2 using TiO_2 and $\text{SnO}_2@\text{TiO}_2$ as ETLs. (c) The J - V curves obtained by reverse and forward scans for the TiO_2 -based champion cell at the scan step of 23.7 mV and delay time of 100, 500, 1000, as well as 1500 ms under a simulated AM 1.5G solar illumination of 100 mW cm^{-2} . (d) The J - V curves obtained at reverse and forward scans for the $\text{SnO}_2@\text{TiO}_2$ -based champion cell at a scan step of 23.7 mV and delay time of 100, 500, 1000, as well as 1500 ms. Normalized (e) transient photovoltage decay and (f) photocurrent decay curves of PSCs with TiO_2 as well as $\text{SnO}_2@\text{TiO}_2$ as ETLs.

the PCE statistical graph of the devices based on TiO_2 ETLs and $\text{SnO}_2@\text{TiO}_2$ ETLs (72 devices in total). Other photovoltaic parameters are shown in Fig. S6b–d (ESI†). The average PCE is significantly improved from $19.55 \pm 0.51\%$ to $21.22 \pm 0.44\%$ at the reverse scan using $\text{SnO}_2@\text{TiO}_2$. Interestingly, we found that both devices with TiO_2 and $\text{SnO}_2@\text{TiO}_2$ ETLs showed an ultra-high fill factor of $\sim 82\%$, generally higher than that of the devices based on spin-coated ETLs.^{25,28} We ascribed this to the ETL conformally growing on the surface of the FTO films *via* the chemical bath method; this morphology ensured a good contact between FTO and ETLs and avoided pinholes and gaps between the ETLs and FTO films always appearing during the spin-coating process. Furthermore, the very small thickness of $\sim 30 \text{ nm}$ (Fig. 3g) of the ETL ensures a small resistance. Among the 36 devices that used TiO_2 ETLs, the champion cell achieves an efficiency of 20.72% (at the reverse scan), measured by the reverse and forward scans at the scan step of 23.7 mV and delay times of 100, 500, 1000, and 1500 ms at each point under a simulated AM 1.5G solar illumination of 100 mW cm^{-2} (Fig. 4c). All the photovoltaic parameters are listed in Table S2 (ESI†). It is apparent that the reverse scan rate hardly influences the PCE; instead, with the decreasing forward scan rate, the PCE increases, but is still much smaller than that obtained under reverse scan; this is a normal phenomenon for planar PSCs with TiO_2 ETLs.^{50,58} Moreover, we found that the device based on the TiO_2 ETL produced current density higher than short-circuit current density at high bias voltages in the J - V curves (Fig. 4c) at the reverse scan, and it could be called current shoulder that was also shown in the literature^{34,56} and possibly caused by the deep trap states on the TiO_2 surface. Using SnO_2 modification, the phenomenon can be alleviated or even eliminated (Fig. S6†). For $\text{SnO}_2@\text{TiO}_2$ ETLs, the champion cell was investigated, as

shown in Fig. 4d. All the photovoltaic parameters are listed in Table S3 (ESI†). The PCE of the champion cell shows little change at different scan rates, and the highest PCE of 21.96% at the reverse scan and 20.57% at the forward scan was obtained with almost no hysteresis. Furthermore, the output photocurrent density (J) and the PCE at maximum power point of the champion cell were measured at a bias voltage of 975 mV. The J stabilized at 22.12 mA cm^{-2} , and PCE stabilized at 21.56% for about 200 s (Fig. S6e, ESI†). Moreover, the incident photon-to-current conversion efficiency (IPCE) of the champion solar cells with TiO_2 ETL and $\text{SnO}_2@\text{TiO}_2$ ETL was measured, as shown in Fig. S6f (ESI†). The integrated J_{SC} of 23.28 mA cm^{-2} for the $\text{SnO}_2@\text{TiO}_2$ -based device is much higher than 20.62 mA cm^{-2} for the TiO_2 -based device. However, the integrated J_{SC} of both devices is slightly smaller than the J_{SC} obtained from the J - V curves measured under one simulated sun illumination; this may be due to the weak response of the devices to monochromatic light with relatively weak intensity especially for the long wavelengths ranging from 740 nm to 850 nm during the measurement of the IPCE.

To investigate the influence of different ETLs on charge transfer and charge recombination of the device, we measured the transient photocurrent decay under short-circuit condition and photovoltage decay under open-circuit condition. As shown in Fig. 4e, the results exhibit that the decay time is $72.60 \mu\text{s}$ for the $\text{SnO}_2@\text{TiO}_2$ -based device, comparable to $71.97 \mu\text{s}$ for the TiO_2 -based device. However, as observed from the transient photocurrent decay measurements, the decay time is significantly reduced from $22.57 \mu\text{s}$ to $2.3 \mu\text{s}$; this indicates that using the SnO_2 -modified TiO_2 film, the charge extraction of the device can be significantly enhanced, thus resulting in a higher J_{SC} . The electrical impedance spectroscopy (EIS) spectra of devices

were obtained and fitted by a circuit consisting of one resistance element and two lumped RC elements in series (Fig. S7a, ESI†). The Nyquist plots of the devices based on TiO_2 and $\text{SnO}_2@\text{TiO}_2$ ETLs at different bias voltages are shown in Fig. S7b and c (ESI†), respectively. The addition of the SnO_2 layer to the TiO_2 layer does not produce an increase in the series resistance (R_s) of the device, as shown in Fig. S7d (ESI†). The charge transfer resistances (R_{CT}) of the $\text{SnO}_2@\text{TiO}_2$ -based device are larger than those of the TiO_2 -based device (Fig. S7e, ESI†); this may be because the ETL becomes thicker upon the addition of the SnO_2 layer. The recombination resistances (R_{CR}) for the charge recombination process at the ETL/perovskite interface⁵⁸ decrease with the increasing bias voltages for two devices (Fig. S7f, ESI†), corresponding to the previous results.⁵⁸ It can be seen that the $\text{SnO}_2@\text{TiO}_2$ -based device displays a larger R_{CR} than the TiO_2 -based device; this demonstrates that the former presents a slower charge recombination process at the ETL/perovskite interface and a larger V_{OC} ,^{59,60} corresponding to the results obtained from the J - V measurements (Fig. S6c, ESI†).

The simple and low-temperature $\text{SnO}_2@\text{TiO}_2$ film is expected to substitute the spin-coated ETLs and can be used for

fabricating large-scale devices, which will benefit the future commercial applications. We then fabricated planar PSCs with an active area larger than one square centimetre. We obtained an average PCE of $18.79 \pm 0.70\%$ at the reverse scan for 36 devices. The PCE statistical graph of the devices is shown in Fig. 5a, and other photovoltaic parameters are shown in Fig. S8a–c (ESI†). Similar to the small-area devices, the large-area devices show high efficiency with high fill factor and excellent reproducibility; this indicates that $\text{SnO}_2@\text{TiO}_2$ films have good uniformity. The best device exhibits a PCE of 20.40% at the reverse scan and 19.18% at the forward scan (Fig. 5b), stabilizing at 20% at maximum power point (Fig. S8d, ESI†). Furthermore, we fabricated solar modules with different active areas. The best solar module shows a PCE of 17.80% at the reverse scan and 16.62% at the forward scan for the device with a masked area of 5.25 cm^2 (Fig. 5c); for a masked area of 10.56 cm^2 , the efficiencies are 16.81% and 15.80% at the reverse and forward scans, respectively (Fig. 5d). The fabrication details of the solar module are shown in Fig. S9 and S10.† Finally, the larger solar modules with a substrate area of 27.5 cm^2 achieved a certified efficiency of 15.65% (15.87% at the reverse scan and

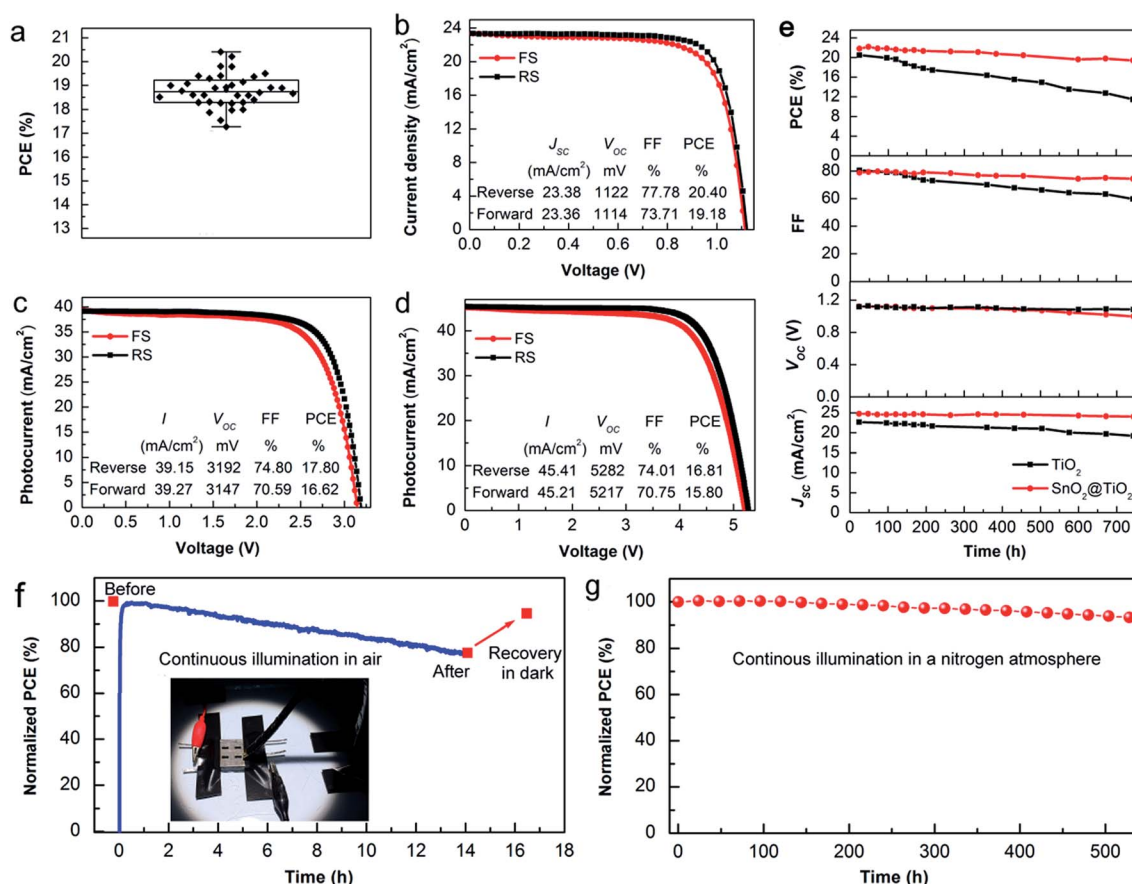


Fig. 5 Device performance and stability test. (a) PCE statistical graph for devices with an active area of 1.13 cm^2 using $\text{SnO}_2@\text{TiO}_2$ as ETLs. (b) The J - V curves obtained by reverse and forward scans for the 1.13 cm^2 champion cell at a scan step of 23.7 mV and delay time of 1000 ms. (c) The J - V curves for the 5.25 cm^2 solar module using $\text{SnO}_2@\text{TiO}_2$ as ETLs. (d) The J - V curves for the 10.56 cm^2 solar module. (e) PCE, FF, V_{OC} as well as J_{SC} of the typical normal planar perovskite devices using TiO_2 and $\text{SnO}_2@\text{TiO}_2$ as ETLs as a function of storage time without encapsulation. (f) Stability test under AM 1.5G light illumination with an intensity of 100 mW cm^{-2} in air with humidity of 45–55% for 14 hours. (g) Stability test under continuous illumination of AM 1.5G light with UV-filter with an intensity of 100 mW cm^{-2} under a nitrogen atmosphere for 528 hours.

15.43% at the forward scan) for perovskite solar modules with a masked area of 10.55 cm^2 (Fig. S11–S14†). Therefore, the $\text{SnO}_2@/\text{TiO}_2$ film has been proven to be a more promising ETL for large-scale perovskite solar cells as compared to other modified ETLs related to SnO_2 , which can also significantly enhance the performance of perovskite solar cells, but still has the demand of spin-coating process or higher cost.^{61–63}

As the PSCs are approaching commercial production, the long-term stability should be another issue of concern.^{7,64} Then, we measured the long-term stability of the planar PSCs with $\text{SnO}_2@/\text{TiO}_2$ and TiO_2 ETLs during about 750 hours of aging. Both devices without encapsulation were stored in an auto-drying cabinet at 20°C with a relative humidity of 15%. The devices were measured in air at a temperature of $22\text{--}25^\circ\text{C}$ and a relative humidity of 45–55%. After 750 hours of ageing, the $\text{SnO}_2@/\text{TiO}_2$ -based device maintained about 89.0% of its initial efficiency, whereas the TiO_2 -based device only maintained about 59.3% of its initial efficiency (Fig. 5e). It can be seen that the main decrease in the PCE of TiO_2 -based devices is caused by the decline of FF owing to the instability of the TiO_2 /perovskite interface especially under UV light exposure.^{15,43,65} Instead, previous results have demonstrated that SnO_2 -based PSCs are very stable.^{47,66,67} Thus, due to the SnO_2 nanoparticle on the TiO_2 film, the trap states at the ETL/perovskite interface are effectively suppressed; this leads to a much more stable interface even after a long time of aging. An unencapsulated $\text{SnO}_2@/\text{TiO}_2$ -based device was aged at maximum power point under a simulated AM 1.5G solar illumination of 100 mW cm^{-2} for 14 h with N_2 flow cooling the surface of the device in air with a relative humidity of 45–55%. As shown in Fig. 5f, the efficiency of the device kept decreasing with time under continuous illumination; after aging, the efficiency decreased to 76.6% of its initial efficiency, which showed much better stability than that of devices tested under air conditions with continuous illumination reported to date.^{68,69} Interestingly, after the aged device was stored in dark for 12 h, the efficiency exhibited recovery to 94.4% of its initial efficiency. The abovementioned results completely correspond to the results of a previous study in which a SnO_2 -based device has been tested.⁴⁷ Moreover, one device was tested under ideal conditions, namely under continuous full-sun illumination without UV-light under a nitrogen atmosphere, as shown in Fig. 5g. Impressively, the $\text{SnO}_2@/\text{TiO}_2$ -based perovskite solar cell showed excellent stability, retaining 93.28% of its initial efficiency after continuous full-sun illumination for 528 hours, better than that for pure TiO_2 -based perovskite solar cells that only retained 90% of their initial efficiency after 500 hours of illumination.²⁶ More importantly, perovskite solar cells require encapsulation to cut off from water and oxygen and thus can obtain much better stability under illumination, which can also be seen in the previous studies.^{68,69}

Conclusions

In summary, we proposed SnO_2 nanoparticle-modified TiO_2 as the ETL in PSCs. Using the simple three-step chemical bath method, the $\text{SnO}_2@/\text{TiO}_2$ film can be successfully fabricated with

a dense, uniform, and pinhole-free morphology. The $\text{SnO}_2@/\text{TiO}_2$ films can significantly enhance the electron extraction and decrease the trap states at the ETL/perovskite interface, effectively suppressing the charge recombination, resulting in reduced hysteresis and superior stability for planar PSCs and attaining an efficiency of higher than 21%. On large solar modules, the $\text{SnO}_2@/\text{TiO}_2$ ETL also boosts an efficiency of 16.81% at the reverse scan. The $\text{SnO}_2@/\text{TiO}_2$ -based perovskite solar cells retained 89.00% and 93.28% of the initial efficiency after about 750 hours of aging in air under darkness and 528 hours under continuous illumination under a nitrogen atmosphere, which thus boosted excellent long-term stability of planar perovskite solar cells. Moreover, the three-step chemical bath method can cause a close contact between the $\text{SnO}_2@/\text{TiO}_2$ layer and the FTO layer and can also be directly transferred to commercial applications. This technique yields thin, but extremely dense ETLs on substrates of any size and removes spin-coating deposition that suffers from thickness, non-uniformity, and substrate size limitations. Furthermore, the $\text{SnO}_2@/\text{TiO}_2$ films can be facilely produced at low temperatures, *i.e.*, less than 140°C , thus offering a promising path to future fabrication of flexible devices. Therefore, the large-scale fabrication of $\text{SnO}_2@/\text{TiO}_2$ ETLs has enormous potential and will take a giant step forward in commercializing perovskite solar cells.

Conflicts of interest

There are no conflicts of interest to declare.

Acknowledgements

The authors acknowledge the financial support received from the National Program for Support of Top-notch Young Professionals. We thank Dr Jun Xi and Mr Zaiyu Wang, and Dr Hao Li for the PL, IPCE testing, as well as transient photovoltage decay and photocurrent decay.

Notes and references

- 1 A. Kojima, K. Teshima, Y. Shirai and T. Miyasaka, *J. Am. Chem. Soc.*, 2009, **131**, 6050–6051.
- 2 M. M. Lee, J. Teuscher, T. Miyasaka, T. N. Murakami and H. J. Snaith, *Science*, 2012, **338**, 643–647.
- 3 National Renewable Energy Laboratory Home Page, <https://www.nrel.gov/pv/assets/images/efficiency-chart.png>.
- 4 M. Saliba, T. Matsui, K. Domanski, J.-Y. Seo, A. Ummadisingu, S. M. Zakeeruddin, J.-P. Correa-Baena, W. R. Tress, A. Abate, A. Hagfeldt and M. Grätzel, *Science*, 2016, **354**, 206–209.
- 5 K. A. Bush, A. F. Palmstrom, Z. J. Yu, M. Boccard, R. Cheacharoen, J. P. Mailoa, D. P. McMeekin, R. L. Z. Hoyer, C. D. Bailie, T. Leijtens, I. M. Peters, M. C. Minichetti, N. Rolston, R. Prasanna, S. Sofia, D. Harwood, W. Ma, F. Moghadam, H. J. Snaith, T. Buonassisi, Z. C. Holman, S. F. Bent and M. D. McGehee, *Nat. Energy*, 2017, **2**, 17009.

- 6 T. Duong, Y. L. Wu, H. Shen, J. Peng, X. Fu, D. Jacobs, E.-C. Wang, T. C. Kho, K. C. Fong, M. Stocks, E. Franklin, A. Blakers, N. Zin, K. McIntosh, W. Li, Y.-B. Cheng, T. P. White, K. Weber and K. Catchpole, *Adv. Energy Mater.*, 2017, 1700228.
- 7 R. F. Service, *Science*, 2016, **354**, 1214–1215.
- 8 J.-W. Lee, D.-H. Kim, H.-S. Kim, S.-W. Seo, S. M. Cho and N.-G. Park, *Adv. Energy Mater.*, 2015, **5**, 1501310.
- 9 M. Saliba, T. Matsui, J.-Y. Seo, K. Domanski, J.-P. Correa-Baena, M. K. Nazeeruddin, S. M. Zakeeruddin, M. Tress, A. Abate, A. Hagfeldt and M. Grätzel, *Energy Environ. Sci.*, 2016, **9**, 1989–1997.
- 10 X. Li, D. Bi, C. Yi, J.-D. Décoppet, J. Luo, S. M. Zakeeruddin, A. Hagfeldt and M. Grätzel, *Science*, 2016, **353**, 58–62.
- 11 B. Ding, L.-L. Gao, L.-S. Liang, Q.-Q. Chu, X.-X. Song, Y. Li, G.-J. Yang, B. Fan, M.-K. Wang, C.-X. Li and C.-J. Li, *ACS Appl. Mater. Interfaces*, 2016, **8**, 20067–20073.
- 12 D. Bi, C. Yi, J. Luo, J.-D. Décoppet, F. Zhang, S. M. Zakeeruddin, X. Li, A. Hagfeldt and M. Grätzel, *Nat. Energy*, 2016, **1**, 16142.
- 13 B. Ding, Y. Li, S.-Y. Huang, Q.-Q. Chu, C.-X. Li, C.-J. Li and G.-J. Yang, *J. Mater. Chem. A*, 2017, **5**, 6840–6848.
- 14 J. You, L. Meng, T.-B. Song, T.-F. Guo, Y. M. Yang, W.-H. Chang, Z. Hong, H. Chen, H. Zhou, Q. Chen, Y. Liu, N. De Marco and Y. Yang, *Nat. Nanotechnol.*, 2016, **11**, 75–81.
- 15 W. Li, W. Zhang, S. V. Reenen, R. J. Sutton, J. Fan, A. A. Haghighirad, M. B. Johnston, L. Wang and H. J. Snaith, *Energy Environ. Sci.*, 2016, **9**, 490–498.
- 16 S. S. Shin, E. J. Yeom, W. S. Yang, S. Hur, M. G. Kim, J. Im, J. Seo, J. H. Noh and S. I. Seok, *Science*, 2017, **356**, 167–171.
- 17 Y. Zhao, J. Wei, H. Li, Y. Yan, W. Zhou, D. Yu and Q. Zhao, *Nat. Commun.*, 2016, **7**, 10228.
- 18 F. Bella, G. Griffini, J.-P. Correa-Baena, G. Saracco, M. Grätzel, A. Hagfeldt, S. Turri and C. Gerbaldi, *Science*, 2016, **354**, 203–206.
- 19 A. Mei, X. Li, L. Liu, Z. Ku, T. Liu, Y. Rong, M. X. M. Hu, J. Chen, Y. Yang, M. Grätzel and H. Han, *Science*, 2014, **345**, 295–298.
- 20 M. Liu, M. B. Johnston and H. J. Snaith, *Nature*, 2013, **501**, 395–398.
- 21 J. Seo, S. Park, Y. C. Kim, N. J. Jeon, J. H. Noh, S. C. Yoon and S. I. Seok, *Energy Environ. Sci.*, 2014, **7**, 2642–2646.
- 22 C. Zuo, H. J. Bolink, H. Han, J. Huang, D. Cahen and L. Ding, *Adv. Sci.*, 2016, **3**, 1500324.
- 23 W. Chen, Y. Wu, Y. Yue, J. Liu, W. Zhang, X. Yang, H. Chen, E. Bi, I. Ashraful, M. Grätzel and L. Han, *Science*, 2015, **350**, 944–948.
- 24 Y. Wu, X. Yang, W. Chen, Y. Yue, M. Cai, F. Xie, E. Bi, A. Islam and L. Han, *Nat. Energy*, 2016, **1**, 16148.
- 25 Q. Jiang, L. Zhang, H. Wang, X. Yang, J. Meng, H. Liu, Z. Yin, J. Wu, X. Zhang and J. You, *Nat. Energy*, 2016, **2**, 16177.
- 26 H. Tan, A. Jain, O. Voznyy, X. Lan, F. P. G. d. Arquer, J. Z. Fan, R. Quintero-Bermudez, M. Yuan, B. Zhang, Y. Zhao, F. Fan, P. Li, L. N. Quan, Y. Zhao, Z.-H. Lu, Z. Yang, S. Hoogland and E. H. Sargent, *Science*, 2017, **355**, 722–726.
- 27 E. Edri, S. Kirmayer, A. Henning, S. Mukhopadhyay, K. Gartsman, Y. Rosenwaks, G. Hodes and D. Cahen, *Nano Lett.*, 2014, **14**, 1000–1004.
- 28 H. Zhou, Q. Chen, G. Li, S. Luo, T.-b. Song, H.-S. Duan, Z. Hong, J. You, Y. Liu and Y. Yang, *Science*, 2014, **345**, 542–546.
- 29 L. Li, Y. Chen, Z. Liu, Q. Chen, X. Wang and H. Zhou, *Adv. Mater.*, 2016, **28**, 9862–9868.
- 30 D. Yang, X. Zhou, R. Yang, Z. Yang, W. Yu, X. Wang, C. Li, S. Liu and R. P. H. Chang, *Energy Environ. Sci.*, 2016, **9**, 3071–3078.
- 31 J. Choi, S. Song, M. T. Horantner, H. J. Snaith and T. Park, *ACS Nano*, 2016, **10**, 6029–6036.
- 32 M. Yang, Y. Zhou, Y. Zeng, C.-S. Jiang, N. P. Padture and K. Zhu, *Adv. Mater.*, 2015, **27**, 6363–6370.
- 33 M. Yang, Z. Li, M. O. Reese, O. G. Reid, D. H. Kim, S. Sio, T. R. Klein, Y. Yan, J. J. Berry, M. F. A. M. v. Hest and K. Zhu, *Nat. Energy*, 2017, **2**, 17038.
- 34 E. L. Unger, E. T. Hoke, C. D. Bailie, W. H. Nguyen, A. R. Bowring, T. Heumuller, M. G. Christoforod and M. D. McGehee, *Energy Environ. Sci.*, 2014, **7**, 3690–3698.
- 35 Y. Zhang, M. Liu, G. E. Eperon, T. C. Leijtens, D. McMeekin, M. Saliba, W. Zhang, M. d. Bastiani, A. Petrozza, L. M. Herz, M. B. Johnston, H. Lin and H. J. Snaith, *Mater. Horiz.*, 2015, **2**, 315–322.
- 36 S. v. Reenen, M. Kemerink and H. J. Snaith, *J. Phys. Chem. Lett.*, 2015, **6**, 3808–3814.
- 37 P. Calado, A. M. Telford, D. Bryant, X. Li, J. Nelson, B. C. O'Regan and P. R. F. Barnes, *Nat. Commun.*, 2016, **7**, 13831.
- 38 H. J. Snaith, A. Abate, J. M. Ball, G. E. Eperon, T. Leijtens, N. K. Noel, S. D. Stranks, J. T. Wang, K. Wojciechowski and W. Zhang, *J. Phys. Chem. Lett.*, 2014, **5**, 1511–1515.
- 39 Y. Li, Y. Zhao, Q. Chen, Y. M. Yang, Y. Liu, Z. Hong, Z. Liu, Y.-T. Hsieh, L. Meng, Y. Li and Y. Yang, *J. Am. Chem. Soc.*, 2015, **137**, 15540–15547.
- 40 A. K. Jena, H.-W. Chen, A. Kogo, Y. Sanehira, M. Ikegami and T. Miyasaka, *ACS Appl. Mater. Interfaces*, 2015, **7**, 9817–9823.
- 41 T. Leijtens, G. E. Eperon, S. Pathak, A. Abate, M. M. Lee and H. J. Snaith, *Nat. Commun.*, 2013, **4**, 2885.
- 42 C. Ludmila, U. Satoshi, P. V. V. Jayaweera, K. Shoji, N. Jotaro, K. Takaya and S. Hiroshi, *Chem. Lett.*, 2015, **44**, 1750–1752.
- 43 S. Ito, S. Tanaka, K. Manab and H. Nishino, *J. Phys. Chem. C*, 2014, **118**, 16995–17000.
- 44 L. Cojocar, S. Uchida, P. V. V. Jayaweera, S. Kaneko, J. Nakazaki, T. Kubo and H. Segawa, *ACS Nano*, 2014, **8**, 12701–12709.
- 45 C. Huang, C. Liu, Y. Di, W. Li, F. Liu, L. Jiang, J. Li, X. Hao and H. Huang, *ACS Appl. Mater. Interfaces*, 2016, **8**, 8520–8526.
- 46 W. Ke, G. Fang, Q. Liu, L. Xiong, P. Qin, H. Tao, J. Wang, H. Lei, B. Li, J. Wan, G. Yang and Y. Yan, *J. Am. Chem. Soc.*, 2015, **137**, 6730–6733.
- 47 E. H. Anaraki, A. Kermanpur, L. Steier, K. Domanski, T. Matsui, W. Tress, M. Saliba, A. Abate, M. Grätzel, A. Hagfeldt and J.-P. Correa-Baena, *Energy Environ. Sci.*, 2016, **9**, 3128–3134.

- 48 H. J. Snaith and C. Ducati, *Nano Lett.*, 2010, **10**, 1259–1265.
- 49 J. P. C. Baena, L. Steier, W. Tress, M. Saliba, S. Neutzner, T. Matsui, F. Giordano, T. J. Jacobsson, A. R. S. Kandada, S. M. Zakeeruddin, A. Petrozza, A. Abate, M. K. Nazeeruddin, M. Grätzel and A. Hagfeldt, *Energy Environ. Sci.*, 2015, **8**, 2928–2934.
- 50 T. Bu, X. Liu, Y. Zhou, J. Yi, X. Huang, L. Luo, J. Xiao, Z. Ku, Y. Peng, F. Huang, Y.-B. Cheng and J. Zhong, *Energy Environ. Sci.*, 2017, **10**, 2509–2515.
- 51 <http://www.microquanta.com/>.
- 52 Q. Tai, P. You, H. Sang, Z. Liu, C. Hu, H. L. W. Chan and F. Yan, *Nat. Commun.*, 2016, **7**, 11105.
- 53 H.-D. Nam, B.-H. Lee, S.-J. Kim, C.-H. Jung, J.-H. Lee and S. Park, *Jpn. J. Appl. Phys.*, 1998, **37**, 4603–4608.
- 54 W. Hu, Y. Liu, R. L. Withers, T. J. Frankcombe, L. Norén, A. Snashall, M. Kitchin, P. Smith, B. Gong, H. Chen, J. Schiemer, F. Brink and J. Wong-Leung, *Nat. Mater.*, 2013, **12**, 821–826.
- 55 F. Ye, H. Chen, F. Xie, W. Tang, M. Yin, J. He, E. Bi, Y. Wang, X. Yang and L. Han, *Energy Environ. Sci.*, 2016, **9**, 2295–2301.
- 56 J. P. C. Baena, L. Steier, W. Tress, M. Saliba, S. Neutzner, T. Matsui, F. Giordano, T. J. Jacobsson, A. R. S. Kandada, S. M. Zakeeruddin, A. Petrozza, A. Abate, M. K. Nazeeruddin, M. Grätzel and A. Hagfeldt, *Energy Environ. Sci.*, 2015, **8**, 2928–2934.
- 57 C. Wang, D. Zhao, C. R. Grice, W. Liao, Y. Yu, A. Cimaroli, N. Shrestha, P. J. Roland, J. Chen, Z. Yu, P. Liu, N. Cheng, R. J. Ellingson, X. Zhao and Y. Yan, *J. Mater. Chem. A*, 2016, **4**, 12080–12087.
- 58 H. Li, W. Shi, W. Huang, E.-P. Yao, J. Han, Z. Chen, S. Liu, Y. Shen, M. Wang and Y. Yang, *Nano Lett.*, 2017, **17**, 2328–2335.
- 59 B. Suarez, V. Gonzalez-Pedro, T. S. Ripolles, R. S. Sanchez, L. Otero and I. Mora-Sero, *J. Phys. Chem. Lett.*, 2014, **5**, 1628–1635.
- 60 O. A. Jaramillo-Quintero, M. S. d. l. Fuente, R. S. Sanchez, I. B. Recalde, E. J. Juarez-Perez, M. E. Rincón and I. Mora-Seró, *Nanoscale*, 2016, **8**, 6271–6277.
- 61 J. Ma, X. Zheng, H. Lei, W. Ke, C. Chen, Z. Chen, G. Yang and G. Fang, *Solar RRL*, 2017, **1**, 1700118.
- 62 L. Xiong, M. Qin, C. Chen, J. Wen, G. Yang, Y. Guo, J. Ma, Q. Zhang, P. Qin, S. Li and G. Fang, *Adv. Funct. Mater.*, 2018, **28**, 1706276.
- 63 G. Yang, C. Chen, F. Yao, Z. Chen, Q. Zhang, X. Zheng, J. Ma, H. Lei, P. Qin, L. Xiong, W. Ke, G. Li, Y. Yan and G. Fang, *Adv. Mater.*, 2018, 1706023.
- 64 Z. Wang, D. P. McMeekin, N. Sakai, S. v. Reenen, K. Wojciechowski, J. B. Patel, M. B. Johnston and H. J. Snaith, *Adv. Mater.*, 2017, **29**, 1604186.
- 65 T. Leijtens, G. E. Eperon, N. K. Noel, S. N. Habisreutinger, A. Petrozza and H. J. Snaith, *Adv. Energy Mater.*, 2015, **5**, 1500963.
- 66 J. Song, E. Zheng, J. Bian, X.-F. Wang, W. Tian, Y. Sanehirac and T. Miyasaka, *J. Mater. Chem. A*, 2015, **3**, 10837–10844.
- 67 B. Roosea, J.-P. C. Baenab, K. C. Gödelc, M. Graetzel, A. Hagfeldtb, U. Steinera and A. Abate, *Nano Energy*, 2016, **30**, 517–522.
- 68 D. Bryant, N. Aristidou, S. Pont, I. Sanchez-Molina, T. Chotchunangatchaval, S. Wheeler, J. R. Durrantab and S. A. Haque, *Energy Environ. Sci.*, 2016, **9**, 1655–1660.
- 69 K. Domanski, E. A. Alharbi, A. Hagfeldt, M. Graetzel and W. Tress, *Nat. Energy*, 2018, **3**, 61–67.